International Journal of Heat and Mass Transfer 52 (2009) 2343–2357

Contents lists available at ScienceDirect

International Journal of Heat and Mass Transfer

journal homepage: www.elsevier.com/locate/ijhmt

Heat flux estimation of a plasma rocket helicon source by solution of the inverse heat conduction problem

James M. Mulcahy [a], David J. Browne [a,*], Kenneth T. Stanton [a], Franklin R. Chang Diaz [b], Leonard D. Cassady [b], Daniel F. Berisford [c], Roger D. Bengtson [c]

[a] School of Electrical, Electronic and Mechanical Engineering, University College Dublin, Belfield, Dublin 4, Ireland
[b] Ad Astra Rocket Company, 141 W. Bay Area Blvd., Webster, Houston, TX 77598, USA
[c] University of Texas, Austin, TX 78712, USA

ARTICLE INFO

Article history:
Received 3 September 2008
Available online 27 January 2009

Keywords:
Inverse problem
Heat flux estimation
Helicon plasma source
VASIMR
Regularization
Steepest descent method

ABSTRACT

A solution of the inverse heat conduction problem (IHCP) by the steepest descent method is carried out in order to determine the waste heat flux from a helicon plasma discharge using transient surface temperature measurements obtained from infrared thermography. The infrared camera data is calibrated against thermocouple data and mapped to real locations on the observed surface. The magnitude and distribution of the heat flux to the gas containment tube in the helicon is investigated as the applied power, gas flow rate, magnetic field distribution and neutral gas are varied.

1. Introduction

1.1. Helicon plasma source

The Variable Specific Impulse Mgnetoplasma Rocket (VASIMR™) under development by Ad Astra Rocket Company, Houston, TX, USA is an advanced space thruster which uses radio waves (RF) to create and accelerate a magnetized plasma to provide thrust. Such a device minimizes wear and erosion due to direct contact between plasma and surfaces and also ejects the propellant at higher velocity than chemical rockets.

The VASIMR™ consists of three sections. The first stage generates plasma from a neutral gas using a helicon source [1]. A helicon source is an efficient plasma generator, producing high density plasmas with a high degree of ionization. Boswell and Chen [2,3] have written a review of helicon research. Helicon devices use an RF power source and antenna operating between the electron and ion cyclotron frequencies to excite electromagnetic waves which damp in the region of maximum density gradient [4,5]. The layout of this first section is shown in Fig. 1. Neutral gas is introduced into a quartz tube which separates the gas from the high voltages on the RF antenna. The helicon antenna is positioned concentrically outside the quartz tube, with a small vacuum gap separating it from the tube outer surface.

Three electromagnetic coils surround the tube and the antenna, hereby referred to as M1, M2 and M3, where M1 is the most upstream magnet and M3 is the most downstream with respect to the direction of propellant flow. These provide the magnetic field required for helicon operation and radial plasma confinement. The annular gap between the quartz tube and the inner surface of the magnets is kept at a vacuum (1.33×10^{-3} Pa) to prevent arcing from the high voltage antenna. A second stage, not shown in Fig. 1, adds further energy to the plasma using radio waves at the ion cyclotron frequency. In the third section, a magnetic nozzle converts azimuthal ion momentum to axial momentum, thereby increasing the ion velocity. The plasma can then detach from the magnetic field.

In this paper, we investigate the thermal behaviour of the high power helicon source used to produce plasma in the VASIMR™ VX-50 laboratory experiment [6]. In converting a neutral gas to a plasma the helicon discharge is subject to a large amount of waste heat due to radiation and particle flux from the plasma. The radiation loss from the helicon plasma is primarily due to UV radiation from resonance transitions in either the neutral or ion. This radiation is absorbed on the surface of the quartz. In addition, further significant energy losses are due to charged particle loss and recombination on the interior of the quartz tube. In order to develop adequate cooling strategies to remove this heat load, it must first be measured. In the experimental set-up, temperature measurements were limited to the external surface of the quartz tube, either through thermocouples attached to the

* Corresponding author. Tel.: +353 1 716 1901; fax: +353 1 283 0534.
E-mail address: david.browne@ucd.ie (D.J. Browne).

0017-9310/$ - see front matter © 2009 Elsevier Ltd. All rights reserved.
doi:10.1016/j.ijheatmasstransfer.2008.10.031

Nomenclature

$A(\theta,z)$	linear correction coefficient for IR data
$B(\theta,z)$	linear correction constant for IR data
$B_M(z)$	axially varying magnetic field strength
C	specific heat
$D^n(\theta,z,t)$	direction of descent at iteration n
I	current in magnets
J	functional to be minimized
∇J	gradient of the functional with respect to change in q_i (θ,z,t)
k	conductivity
L	length of the computational domain
N	no of turns in magnet
n	iteration number
q_a	heat load used to validate inverse method
q_e	estimated heat flux obtained after stopping criterion is met
q_i	true heat flux to inner surface of cylinder
r_i	inner radius
r_o	outer radius
r_m	magnet radius
T	temperature distribution
T_{IR}	uncorrected IR temperature data
T_e^n	outer surface solution of direct problem at iteration n
t_{ps}	start time of known applied heat flux
t_{pf}	end time of known applied heat
t_f	final time in numerical solution of IHCP
Y	measured temperatures at outer surface of tube
β^n	step size at iteration n
Δr	radial spacing
ΔT	variable for solution of sensitivity problem
Δz	axial spacing
$\Delta\theta$	angular spacing
ε_Q	error in heat flux estimation for validation case
ε_T	error in temperature approximation for validation case
μ_0	magnetic permeability of free space
ρ	density
σ	standard deviation of the measuring error
τ	time variable for adjoint problem
ϖ	normally distributed randomly generated number
ψ	variable for solution of adjoint problem

surface or using an IR camera with a window transparent to infrared radiation as shown in Fig. 1. Determining the heat flux from the plasma to the inner surface of the quartz tube using the transient temperature measurements at the external surface is an example of an inverse heat conduction problem.

1.2. Inverse heat conduction problem (IHCP)

A variety of methods for solving the inverse heat conduction problem have been developed over the years. Two of the most researched techniques are the function specification method (FSM) developed by Beck et al. [7] and the iterative regularisation method developed by Alifanov [8]. A comparison of the various methods was carried out by Beck et al. [9]. The iterative regularisation method is a flexible and powerful technique which can be used to determine internal heat sources [10], unknown varying thermo-physical properties [11] and unknown boundary conditions [12,13]. Huang and Wang describe a method to determine an unknown boundary heat flux in an arbitrary 3D domain [14]. The technique approaches the IHCP as an optimisation problem. For the problem discussed in this paper, the objective is to determine an unknown heat flux at an inner surface when the outer surface temperature response is known from measurements. The iterative regularisation technique assumes an arbitrary initial heat flux and solves the direct heat conduction problem to get the temperature response at the outer surface. This temperature response is compared with the measured temperatures and the heat flux is iteratively modified to minimize the difference between them. A number of different methods have been used carry out the optimisation process. A popular technique is the conjugate gradient method which has been investigated for a number of different implementations by Colaco and Orlande [15]. This method has been applied to a three dimensional problem by Loulou and Artioukhine [16]. A conceptually simpler implementation based on the steepest descent method (SDM) was used by Huang and Lo to estimate the heat flux in a cutting tool tip [17] and in a high speed motor housing [18]. In this study, for simplicity, the steepest descent method (SDM) is used to solve the inverse heat conduction problem for a three dimensional hollow cylinder. The solution time using the steepest descent method was sufficiently quick for this

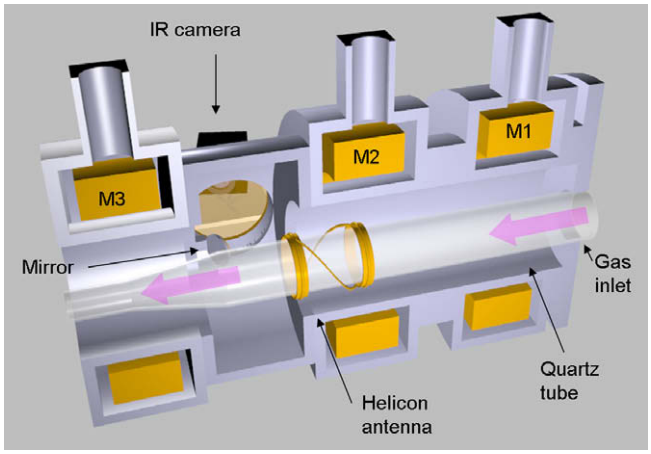

Fig. 1. Layout of quartz tube and helicon antenna inside VASIMR™ VX-50.

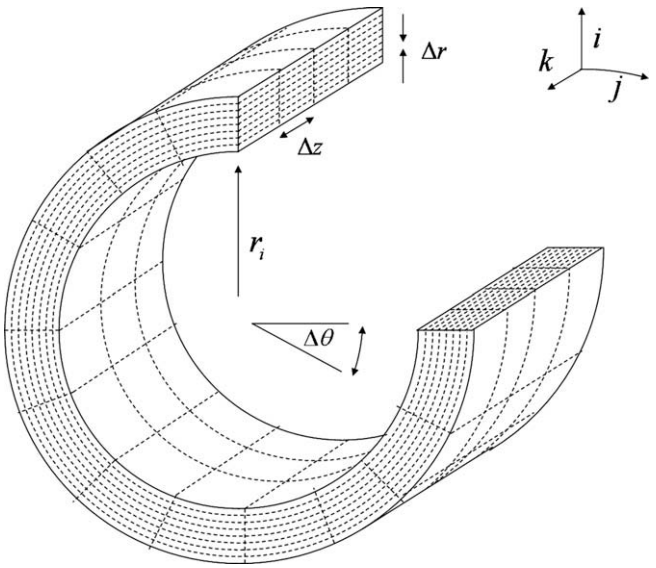

Fig. 2. Computational domain of the inverse problem.

Table 1
Thermo-physical properties of quartz tube.

ρ [kg/m^3]	k [W/mK]	C_P [J/kg K]
2200	1.4	670

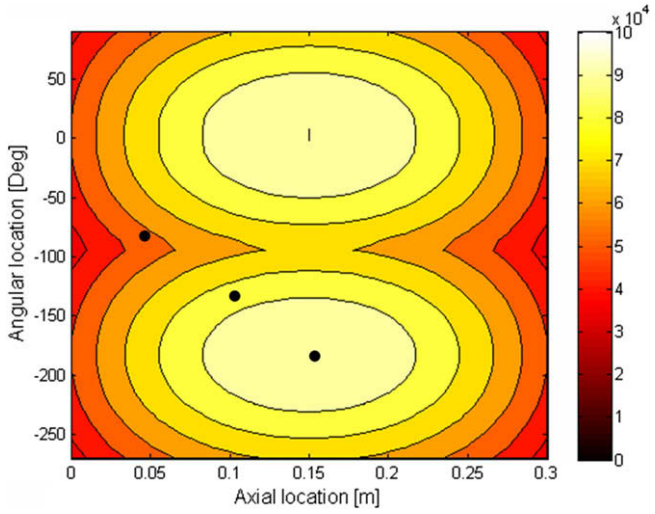

Fig. 3. Spatial distribution of the peak heat flux for the computational test cases.

investigation, and using the conjugate gradient method to improve the convergence time of the solution was not considered necessary.

2. Inverse problem

For the cylindrical geometry being considered, and assuming constant thermo-physical properties, the direct heat conduction equation is given by

$$\rho C\frac{\partial T}{\partial t}=k\left[\frac{\partial^2 T}{\partial r^2}+\frac{1}{r}\frac{\partial T}{\partial r}+\frac{1}{r^2}\frac{\partial^2 T}{\partial \theta^2}+\frac{\partial^2 T}{\partial z^2}\right], \tag{1}$$

$$-k\frac{\partial T(r,\theta,z,t)}{\partial r}=0, \quad \text{at } r=r_o \;\forall\; \theta,z \text{ and } t, \tag{1a}$$

$$-k\frac{\partial T(r,\theta,z,t)}{\partial r}=q_i(\theta,z,t) \quad \text{at } r=r_i, \tag{1b}$$

$$-k\frac{\partial T(r,\theta,z,t)}{\partial z}=0, \quad \text{at } z=0, \text{ and } z=L \;\forall\; \theta,z \text{ and } t, \tag{1c}$$

$$T(r,\theta,z,t)=T_i \quad \text{at } t=0 \;\forall\; \theta,z \text{ and } r. \tag{1d}$$

A schematic of the computational domain of the problem is shown in Fig. 2. In this problem, the heat flux $q_i(\theta,z,t)$ applied to the interior surface of the cylinder is unknown. A heat flux of zero is assumed at the outer radius of the tube, as shown by Eq. (1a). This is deemed to be an acceptable approximation as the temperatures in the experiment do not lead to significant radiation losses from

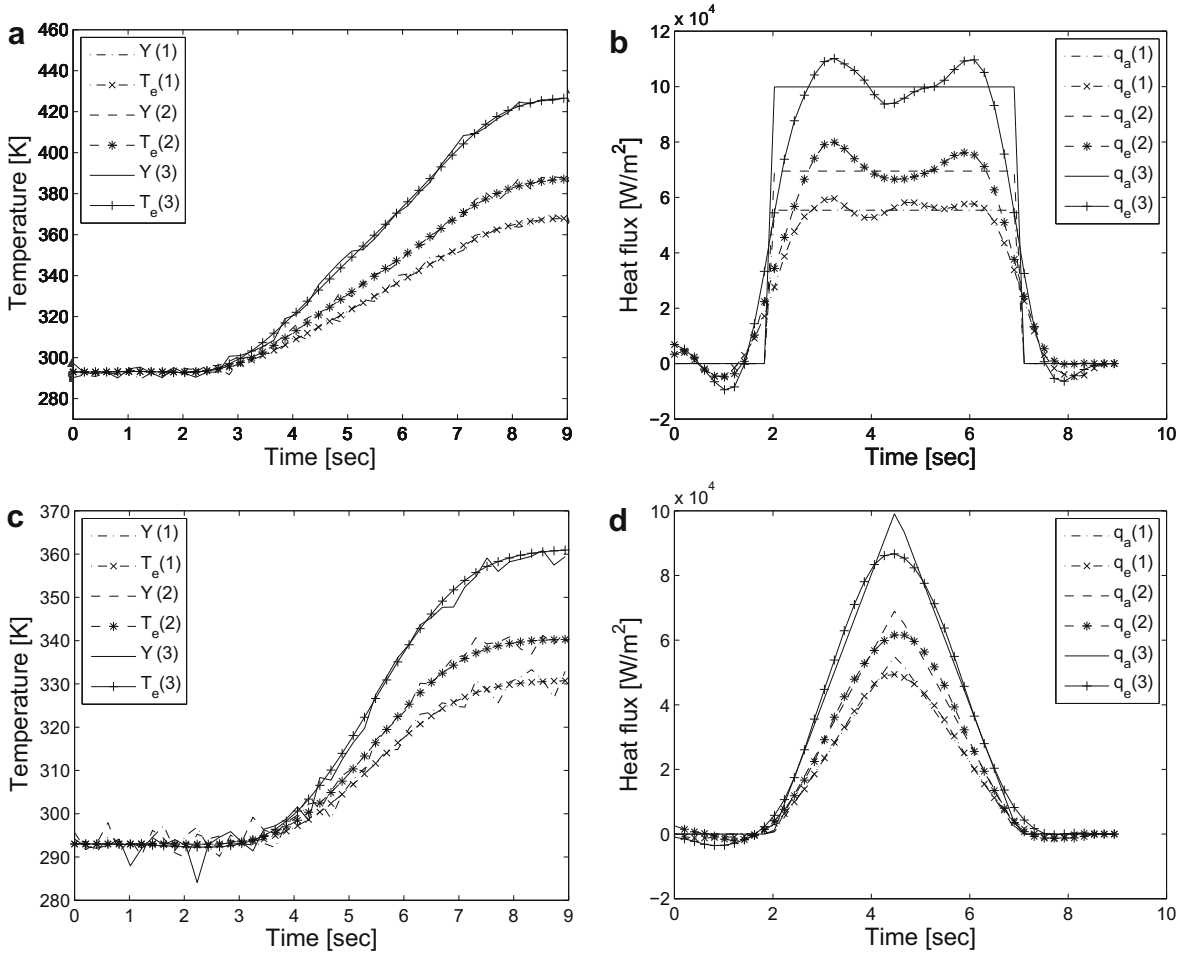

Fig. 4. Comparison of actual and estimated temperatures (a), (c) and heat fluxes (b), (d) for computational test case at locations (0.05 m, 90°), (0.1 m, 135°) and (0.15 m, 180°).

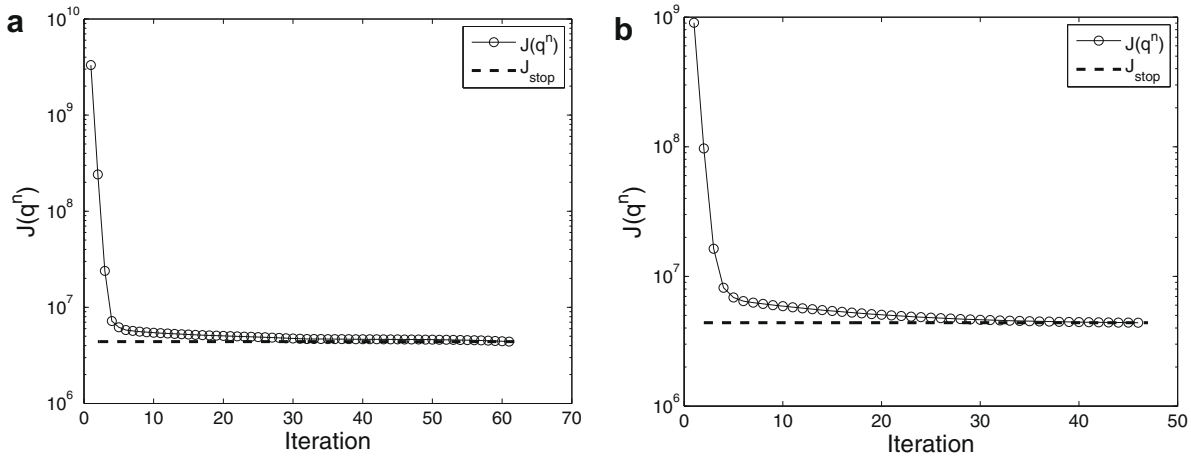

Fig. 5. Variation of the functional J with respect to iteration number for estimating a step heat input (a) and a ramp heat input (b).

the surface. A perfectly insulated boundary is assumed at the axial boundary nodes, as indicated by Eq. (1c). Again this is reasonable as there is such a small area available for axial conduction at this boundary. The temperatures at the outer surface of the tube are known from experimental data obtained from an IR camera or thermocouples. The initial temperature is taken from experimental measurements, Eq. (1d). The aim of the inverse solution is to iteratively estimate the heat flux using an optimisation procedure which results in a negligible difference between the measured temperatures at the outer surface of the tube and estimated temperatures produced by the numerical model. This is done by minimizing the following functional.

$$J^{n+1}(q_i(\theta,z,t)) = \int_0^{t_f}\int_{z_r}^{z_l}\int_0^{2\pi} [T^{n+1}(r_o,\theta,z,t) - Y(\theta,z,t)]^2 d\theta \cdot dz \cdot dt. \tag{2}$$

In the above expression, $T^n(r_o,\theta,z,t)$ is the computed temperature response on the external surface of the tube given by the

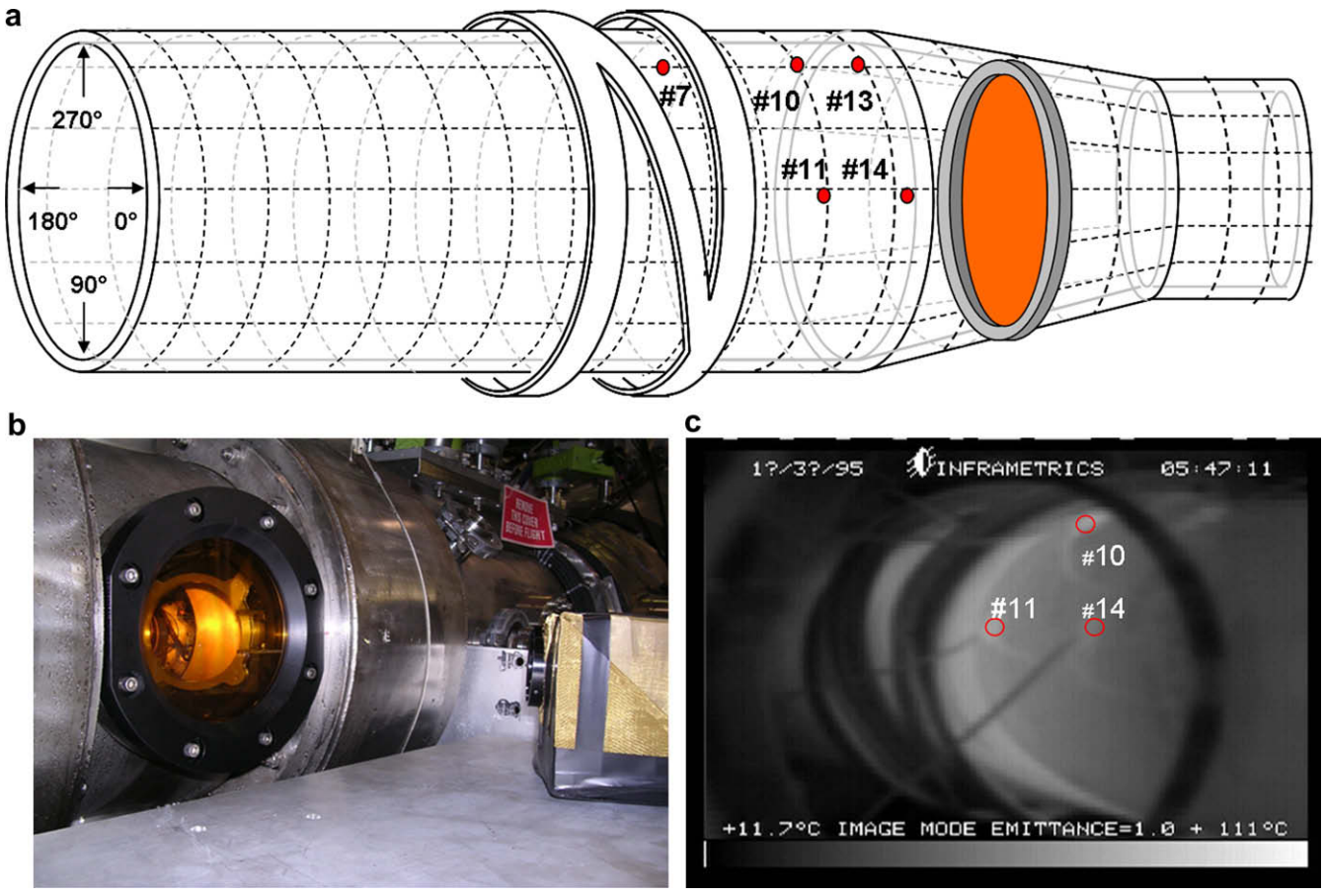

Fig. 6. (a) Layout of thermocouples in experimental set-up. (b) Exterior view of IR camera access. (c) Image from IR camera.

solution of the direct heat transfer problem described by Eq. (1) subject to boundary conditions in Eqs. (1a)–(1d). The variable $Y(\theta,z,t)$ is the measured transient temperature distribution on the tube surface.

3. Steepest descent method

The iterative process by which the functional $J^n(q_i(\theta,z,t))$ is minimized is known as the steepest descent method [8]. It is represented by the following expression for iteratively recalculating the unknown heat flux

$$q_i^{n+1}(\theta,z,t) = q_i^n(\theta,z,t) - \beta^n D^n(\theta,z,t). \tag{3}$$

For each iteration n, the heat flux is adjusted by the direction of descent $D^n(\theta,z,t)$ multiplied by a step size β^n. The direction of descent is given by the gradient of the functional $J(q_i^n(\theta,z,t))$ with respect to changes in $q_i^n(\theta,z,t)$, such that

$$D^n(\theta,z,t) = \nabla J(q_i^n(\theta,z,t)). \tag{4}$$

In order to obtain the gradient of the functional, a solution to what is known as the adjoint problem is required, an explanation of which is given in Section 3.1. In order to obtain the suitable step size a sensitivity problem must be solved. This is explained in Section 3.2.

3.1. Adjoint problem

Based on the perturbation principle Alifanov [8] showed that the gradient of the functional J can be calculated as follows:

$$\nabla J^n(q_i(\theta,z,t)) = -\frac{\psi(r_i,\theta,z,t)}{k}, \tag{5}$$

where $\psi(r_i,\theta,z,t)$ is the solution of the adjoint problem given by

$$-\rho C\frac{\partial\psi}{\partial t} = k\left[\frac{\partial^2\psi}{\partial r^2} + \frac{1}{r}\frac{\partial\psi}{\partial r} + \frac{1}{r^2}\frac{\partial^2\psi}{\partial\theta^2} + \frac{\partial^2\psi}{\partial z^2}\right], \tag{6}$$

$$-k\frac{\partial\psi(r,\theta,z,t)}{\partial r} = 2[T(r_o,\theta,z,t) - Y(\theta,z,t)], \quad \text{at } r = r_o \;\forall\; \theta,z \text{ and } t, \tag{6a}$$

$$-k\frac{\partial\psi(r,\theta,z,t)}{\partial r} = 0, \quad \text{at } r = r_i \;\forall\; \theta,z \text{ and } t, \tag{6b}$$

$$-k\frac{\partial\psi(r,\theta,z,t)}{\partial z} = 0, \quad \text{at } z = 0 \text{ and } z = L \;\forall\; r,\theta \text{ and } t, \tag{6c}$$

$$\psi(r,\theta,z,t) = 0, \quad \text{at } t = t_f \;\forall\; \theta,z \text{ and } r. \tag{6d}$$

There is no initial condition for the adjoint problem, but instead a condition for the final time t_f. By introducing a new time variable defined as $\tau = t_f - t$ the above equations for the adjoint problem are transformed to the same form as the direct problem, and can be solved by the same method.

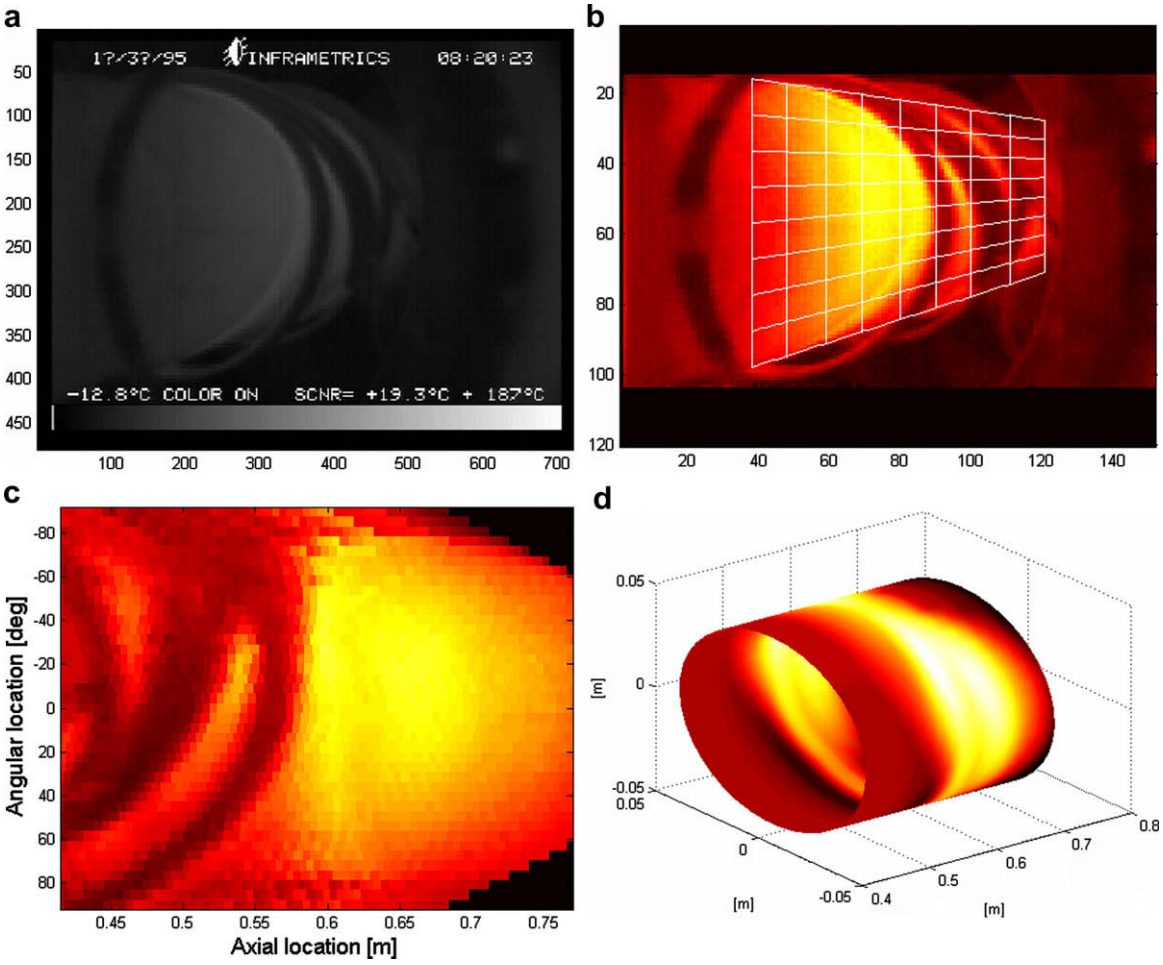

Fig. 7. (a) Image obtained from IR camera. (b) Image with mapping grid overlaid. (c) Image adjusted for tube curvature and perspective. (d) Temperatures mapped to axial and angular positions on tube surface.

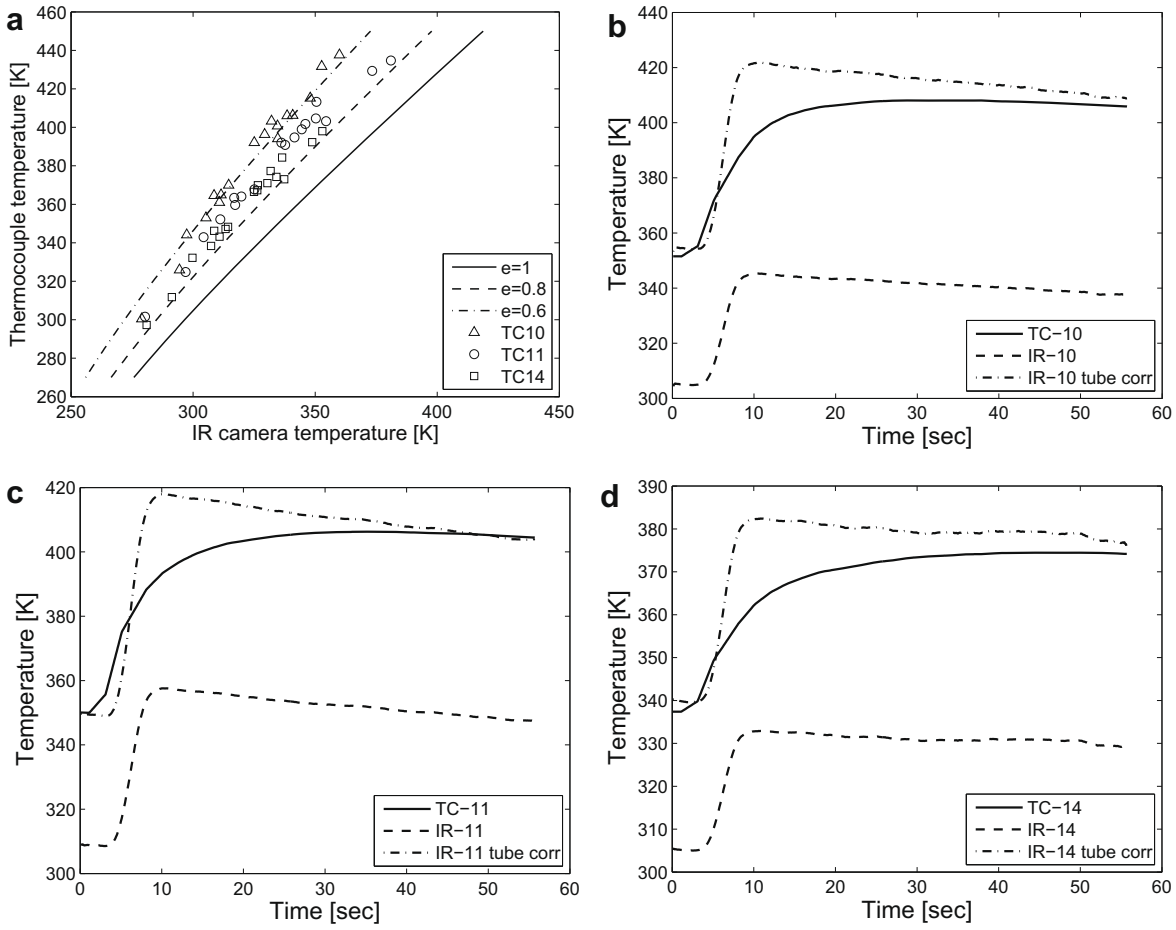

Fig. 8. (a) Thermocouple temperature versus IR camera temperature at locations 10, 11 and 14. Thermocouple, uncorrected and corrected IR camera measurements for locations 10 (b), 11 (c) and 14 (d).

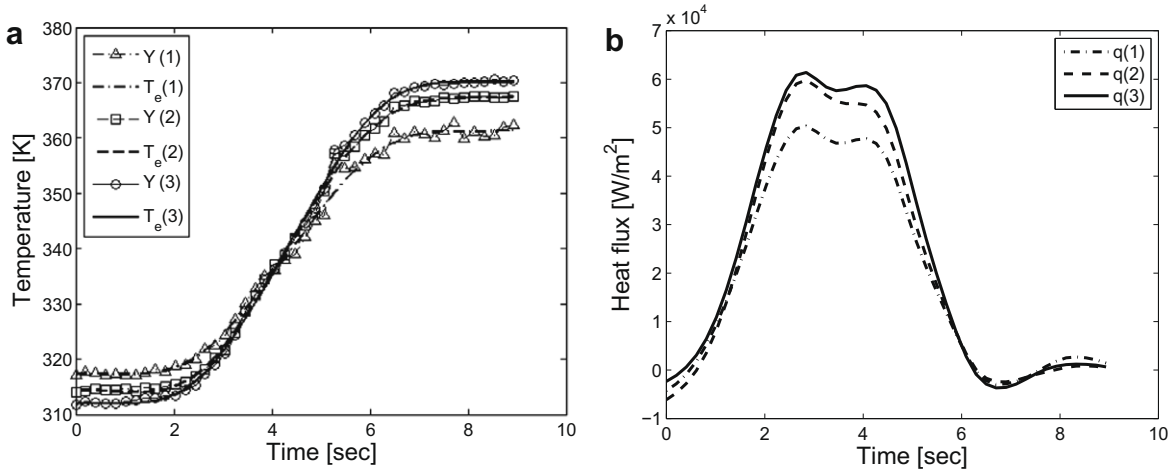

Fig. 9. (a) Comparison of measured and estimated temperatures after the stopping criterion is reached. (b) Time dependent heat flux at single point calculated from temperature data.

3.2. The sensitivity problem

A variation in the applied heat flux Δq will cause a corresponding change in the temperature field such that T becomes $T + \Delta T$. The sensitivity problem is solved by obtaining a solution to the direct heat conduction problem for the perturbation in applied heat flux Δq, which gives the following formulation of the sensitivity problem:

$$\rho C \frac{\partial \Delta T}{\partial t} = k\left[\frac{\partial^2 \Delta T}{\partial r^2} + \frac{1}{r}\frac{\partial \Delta T}{\partial r} + \frac{1}{r^2}\frac{\partial^2 \Delta T}{\partial \theta^2} + \frac{\partial^2 \Delta T}{\partial z^2}\right], \tag{7}$$

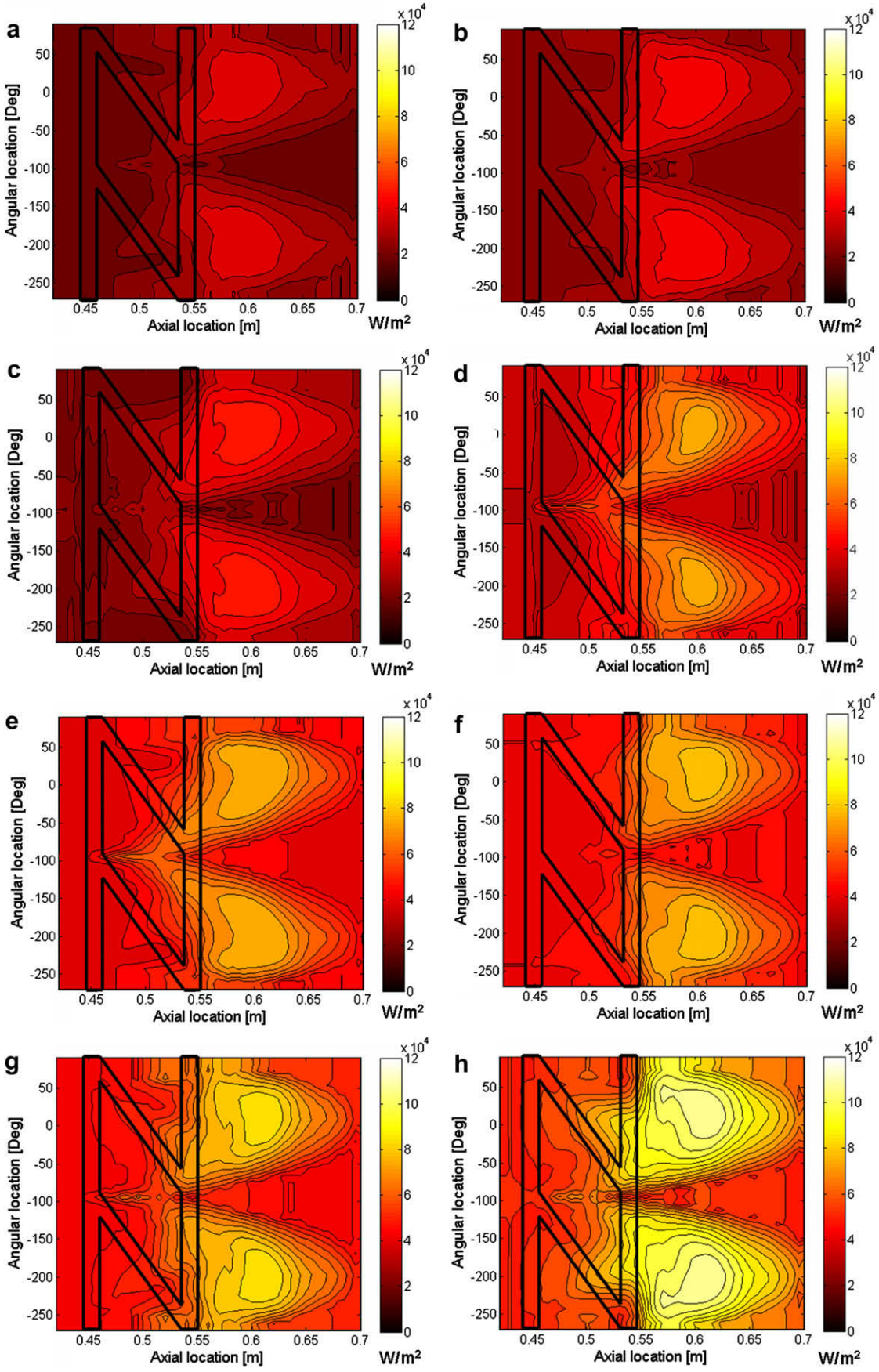

Fig. 10. Average heat flux distribution to inner surface of tube as power applied to the helicon antenna is increased. (a) RF power: 5800 W, (b) RF power: 6000 W, (c) RF power: 6300 W, (d) RF power: 8900 W, (e) RF power: 9300 W, (f) RF power: 12,000 W, (g) RF power: 12,800 W, (h) RF power: 16,200 W.

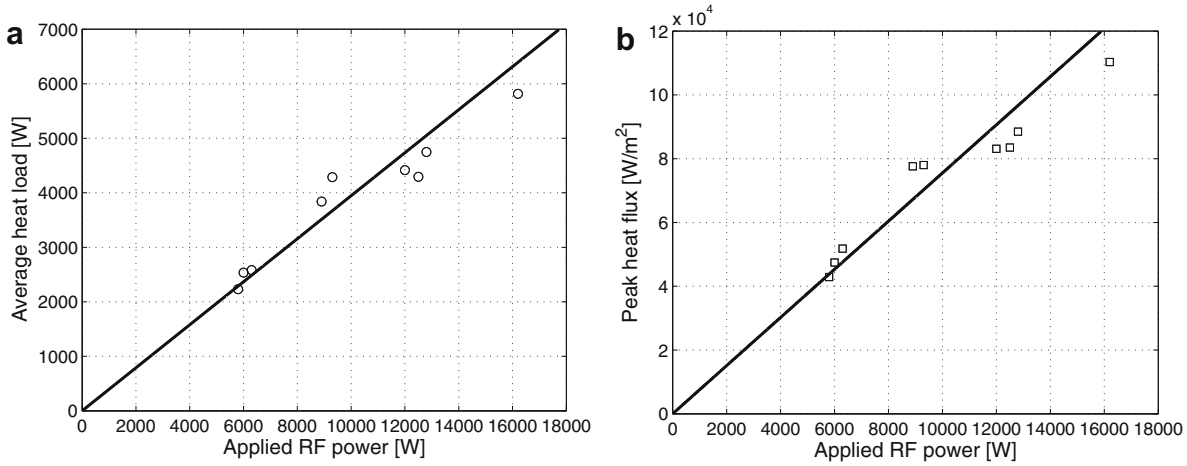

Fig. 11. (a) Heat load versus applied RF power. (b) Peak heat flux versus applied RF power.

$$-k\frac{\partial \Delta T(r,\theta,z,t)}{\partial r}=0, \quad \text{at } r=r_o \;\forall\; \theta,z \text{ and } t, \tag{7a}$$

$$-k\frac{\partial \Delta T(r,\theta,z,t)}{\partial r}=\Delta q, \quad \text{at } r=r_i \;\forall\; \theta,z \text{ and } t, \tag{7b}$$

$$-k\frac{\partial \Delta T(r,\theta,z,t)}{\partial z}=0, \quad \text{at } z=0 \text{ and } z=L \;\forall\; r,\theta \quad \text{and } t, \tag{7c}$$

$$\Delta T(r,\theta,z,t)=0, \quad \text{at } t=0 \;\forall\; \theta,z \text{ and } r. \tag{7d}$$

For the sensitivity problem, the perturbation to the heat flux is the direction of descent given by Eq. (5). For a linear relationship between heat flux and temperature, the change in heat flux at each iteration results in a corresponding change in the temperature distribution given by the following equations:

$$q_i^{n+1}(\theta,z,t)=q_i^n(\theta,z,t)-\beta^n\Delta q_i^n(\theta,z,t), \tag{8}$$

$$T^{n+1}(r_o,\theta,z,t)=T^n(r_o,\theta,z,t)-\beta^n\Delta T^n(r_o,\theta,z,t). \tag{9}$$

Substituting Eq. (9) into Eq. (2), to calculate J for the $n+1$ iteration we get Eq. (10)

$$J^{n+1}(q(\theta,z,t))=\int_0^{t_f}\int_{z_r}^{z_l}\int_0^{2\pi}[T^n(r_o,\theta,z,t)-\beta^n\Delta T^n(r_o,\theta,z,t)-Y(\theta,z,t)]^2 d\theta\, dz\, dt. \tag{10}$$

Minimizing the function J with respect to step size β gives the following expression for β [8]:

$$\beta^n=\frac{\int_0^{t_f}\int_{z_r}^{z_l}\int_0^{2\pi}[T^n(r_o,\theta,z,t)-Y(\theta,z,t)]\Delta T^n(r_o,\theta,z,t)d\theta\, dz\, dt}{\int_0^{t_f}\int_{z_r}^{z_l}\int_0^{2\pi}[\Delta T^n(r_o,\theta,z,t)]^2 d\theta\, dz\, dt}. \tag{11}$$

Table 2
Waste heat load versus applied RF power.

RF power [W]	Waste heat as % of applied power
5800	38.5
6000	42.3
6300	40.9
8900	43.2
9300	46.1
12,000	36.8
12,500	34.4
12,800	37.1
16,200	35.9

3.3. The stopping criterion

The discrepancy principle is used to stabilize the solution of the IHCP from measurement errors [8]. A number of variations on the stopping criterion exist in the literature. In this experiment Eq. (12) was used as the stopping criterion [12]:

$$J<\int_0^{t_f}\int_{2y}^{2l}\int_0^{2\pi}\sigma^2 d\theta\cdot dz\cdot dt, \tag{12}$$

where σ is the standard deviation of the noise error in measured temperature data.

4. Computational procedure

To start the computational procedure an arbitrary heat flux is assumed and the direct problem is solved. In this procedure the heat flux is initially assumed to be zero. The computational procedure is outlined as follows:

1. Solve the direct problem given by Eq. (1).
2. Examine the stopping criterion given by Eq. (12). Continue if not satisfied.
3. Solve the adjoint problem given by Eq. (6).
4. Compute the direction of descent from Eq. (5).
5. Solve the sensitivity problem from Eq. (7), setting $\Delta q = D^n$.
6. Get step size β^n from Eq. (11).
7. Calculate new heat flux q^{n+1} from Eq. (3).
8. Update the calculated temperature using Eq. (9) and return to step 2.

As the heat conduction equation is linear the direct problem only needs to be solved at the first iteration. For subsequent iterations the temperature can be calculated from Eq. (9). Further details can be found in [12].

4.1. Solution of direct problems

For the experimental data involved the plasma was generated for 5 s pulses. The solution of the direct problem was carried out using an explicit finite difference formulation of the partial differential equations involved. A minimum resolution of 0.005 m was chosen in the axial direction, $\Delta z = 0.005$ m. The number of axial nodes is 60. The number of tangential nodes was set to 40, $\Delta\theta = 0.157$ rad, while 10 radial nodes were used, $\Delta r = 0.00025$ m.

The cylindrical quartz tube had $r_i = 45$ mm and an $r_o = 47.5$ mm. The properties of quartz are given in Table 1. The domain is divided into radial, angular and axial nodes $10 \times 40 \times 60$. For stability, the maximum time-step was set to 0.0102 s [19]. Experimental measurements indicated that the tube generally did not have a uniform initial temperature distribution. For the computational procedure the initial temperature distribution is take from the IR measurement at $t = 0$ as shown by Eq. (13). The temperature through the thickness of the tube was assumed to be the same as the outer surface temperature. The numerical solution was validated against test cases where analytical solutions were available from a standard textbook [20]

$$T(r, \theta, z, 0) = Y(\theta, z, 0) \ \forall \ r. \tag{13}$$

5. Computational test cases

In order to evaluate the accuracy of the solution of the inverse problem, simulated data is obtained by solving the direct heat conduction problem with a specified heat flux and using the returned temperature data as the input measurements to the inverse problem.

The known heat flux varies with space and time. The spatial distribution of the heat flux is given by Eq. (14a)

$$q_a(\theta, z, t) = q_{pk}\left(-\frac{2}{L^2}z^2 + \frac{2}{L}z + 0.5\right)(0.7 + 0.3\cos(\theta)), \quad \text{for } t_{ps} \le t \le t_{pf}, \tag{14a}$$

$$q_a(\theta, z, t) = 0 \quad \text{for } t > t_{ps} \text{ and } t < t_{pf}. \tag{14b}$$

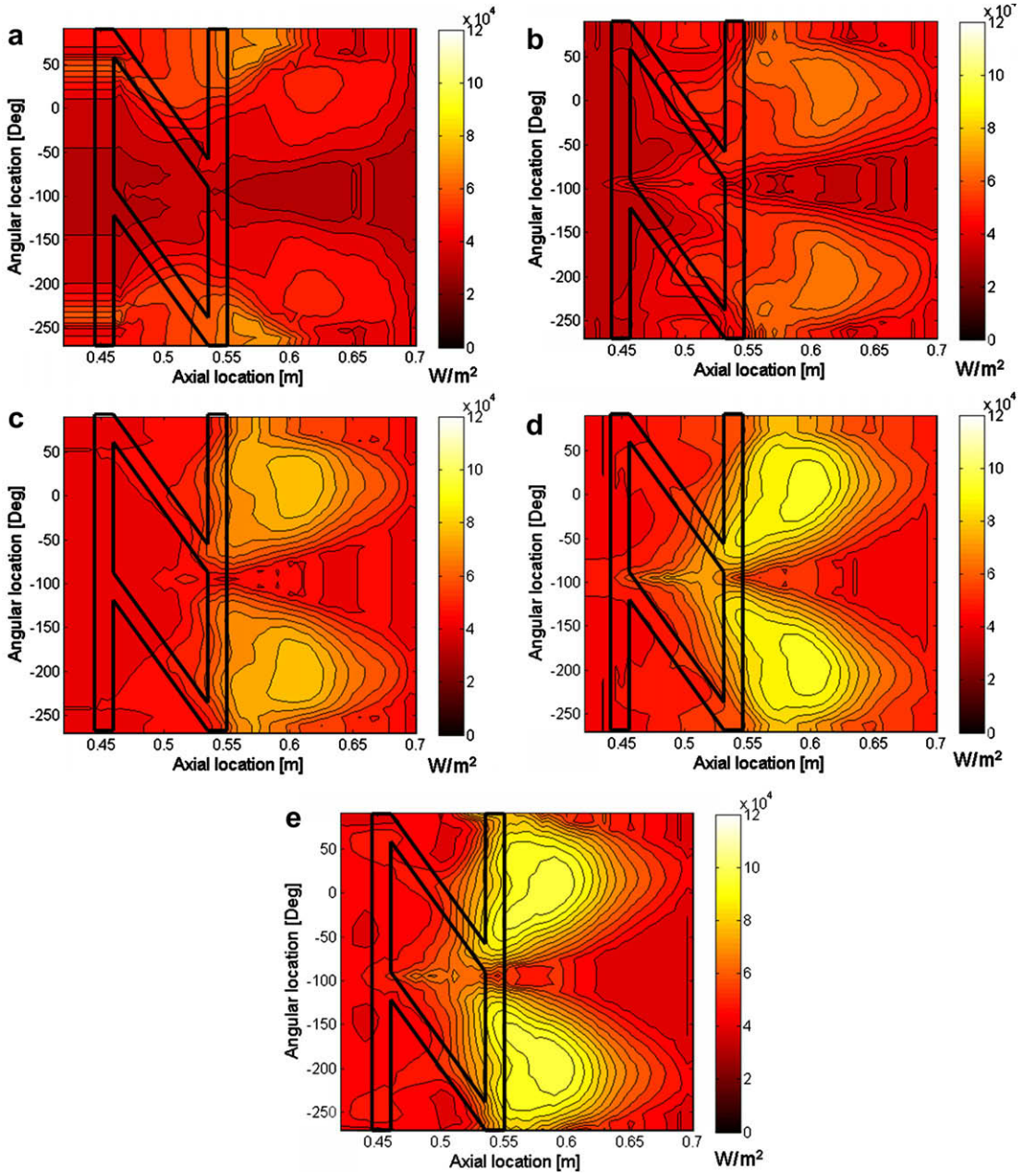

Fig. 12. Average heat flux distribution from the plasma for varying neutral gas flow rate from (a) 5×10^{-6} m^3/s to (e) 1.83×10^{-5} m^3/s. (a) Gas flow rate 5×10^{-6} m^3/s, (b) gas flow rate 8.33×10^{-6} m^3/s, (c) gas flow rate 1.16×10^{-5} m^3/s, (d) gas flow rate 1.5×10^{-5} m^3/s, (e) gas flow rate 1.83×10^{-5} m^3/s.

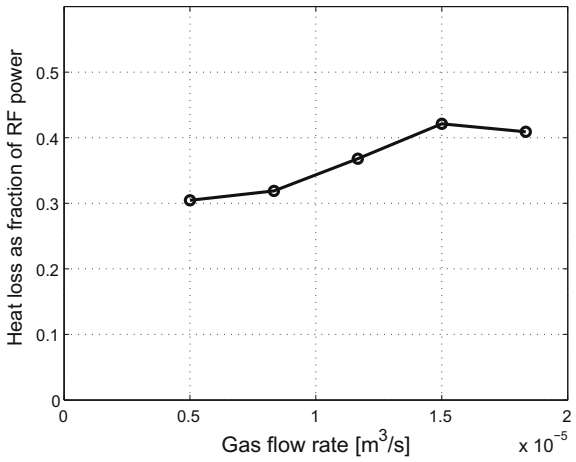

Fig. 13. Heat load as percentage of applied power versus gas flow rate.

To match the experimental data the heat flux was assumed to act over a 5 s pulse. The temporal behaviour of the heat flux was investigated for two cases. In the first one a step behaviour is assumed for time so that heat flux is on between two points in time t_{ps} and t_{pf} and is zero at all other points in time. A peak heat flux q_{pk} of 100 kW/m^2 is used with $t_{ps} = 2$ and $t_{pf} = 7$. For the second case a ramp change was used. The heat flux increases linearly from zero at $t = 2$ to the local maximum at $t = 4.5$, before decreasing linearly to zero at $t = 7$. The length of the computational domain L is set to 0.3 m. The distribution of this heat flux can be seen in Fig. 3. To better approximate real experimental conditions noise is added to the generated temperature measurements using a normally distributed randomly generated number ϖ and a standard deviation σ of 2 K as shown in Eq. (15)

$$Y = T + \bar{\omega}\sigma. \tag{15}$$

The accuracy of the solution of the inverse problem in terms of matching the applied heat flux and the simulated temperature data is evaluated using Eqs. (16) and (17), as follows:

$$\varepsilon_Q = \frac{\sum_{i=1}^{N}\sqrt{(q_e - q_a)^2}}{\sum_{i=1}^{N}\sqrt{(q_a)^2}} \times 100, \tag{16}$$

$$\varepsilon_T = \frac{\sum_{i=1}^{N}\sqrt{(T_e - Y)^2}}{\sum_{i=1}^{N}\sqrt{(Y)^2}} \times 100, \tag{17}$$

where N is the total number of measurements, which is the number of tangential nodes by axial nodes by the number of time-steps. The total time in the applied test case was 9 s and N is 1,099,880. Fig. 4 compares the measured and estimated temperatures, Y and T_e, and the applied and estimated heat fluxes, q_a and q_e, after the stopping criterion has been reached, at three points (0.05 m 90°), (0.1 m 135°) and (0.15 m 180°). The error in the estimation of heat flux for the step change in heat flux from Eq. (16) is 16.47%, while the error in temperature comparison using Eq. (17) is 0.48%. For the ramp change in heat flux the error in the temperature match is 0.51% and the error in matching the heat flux is 7.72%. It can be seen that in general the error in the heat flux data is much larger than in the temperature data. This is due to the ill-posed nature of the inverse heat conduction problem. The estimated heat flux better matches the ramp change than the step change. Fig. 4(b) indicates that that the bulk of the error in the first case is due to poor matching of the sudden change in heat flux that occurs at 2 and 7 s. The second case has a lower heat flux estimation error as the heat flux changes at a slower rate and it is clear form Fig. 4(d) that attains a closer match to the temporal behaviour of the heat flux. The stopping criterion is met after 62 iterations for the first case and after 47 iterations for the second case. The variation of the functional J with respect to the iteration number for each test case is shown in Fig. 5.

6. Temperature measurements

In the experimental set-up, temperature measurements were taken using an IR camera which viewed the outer surface of the quartz tube through a zinc selenide window, which is transparent to infrared radiation at the wavelengths of interest. The Inframetrics model 600 camera has a liquid nitrogen cooled micro-bolometer detector and a spectral bandpass from 8 to 14 μm. The temperature accuracy of the camera is ±2% of the reading. The temperature range of the camera can be adjusted to 5, 10, 20, 50, 100 and 200 K. Temperature measurements were also taken using an array of up to 20 K-type thermocouples which were attached to the surface of the quartz tube using a ceramic adhesive. The experimental layout can be seen in Fig. 6. A gold plated mirror attached inside the vacuum chamber reflected the tube image to allow the camera to view the tube surface from an oblique angle through the IR window. This set-up allowed the IR camera to view the area from the helicon antenna to the start of the taper in the quartz tube. Initial data indicated that this was where the bulk of the heat was deposited. The video output from the IR camera was captured to PC using a DAQ board and National Instruments Labview software. Temperature data was sampled at a rate of 30 Hz. For the inverse method the outer surface temperatures as a function of position and time were required. A Matlab script was written to take images retrieved from the IR video data and, using information known about the geometry, map the pixel data to discrete points on the tube surface as a function of time. The script only took pixels from areas of interest on the surface of the tube, removing areas obscured by the antenna, and interpolating to replace missing values. This procedure introduces some unavoidable uncertainty into the estimation of heat flux. However, the error is believed to be relatively small as the bulk of the heat is known to be deposited downstream of the antenna and the distances over which data is interpolated are relatively small with respect to the total measured area. The script allowed variable spatial and temporal discretization of the temperature data, which allowed the measurement data to match the chosen computational domain. Fig. 7(a)–(d) shows the procedure for taking the image from the IR camera mapping it to the tube surface. To give data for a full cylinder, symmetry is assumed by letting the temperature

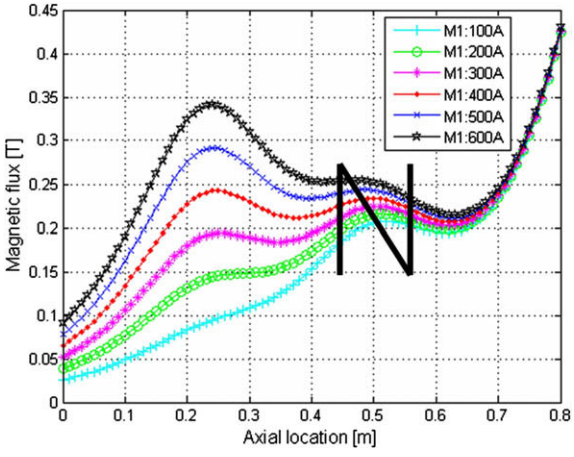

Fig. 14. Magnetic field strength versus axial location with varying M1.

distribution on the unseen side of the cylinder equal that of the visible side. The temperature data from the IR camera contains noise error. For a typical data sample, using 100 K range on the IR camera, the standard deviation of this noise error in the temperature data was determined to be 2.79 K. Measurement of this value is required for calculating the stopping criterion from Eq. (12).

7. Comparison of IR camera and thermocouple data

For calculating the temperature of the quartz tube, the video software in the IR camera assumed the surface to be a black body. In fact the radiation seen by the IR camera will be modified by a number of factors. The zinc selenide window transmits 70% of the IR radiation in the wavelength range of interest. The ambient surroundings at a temperature of 293 K will also contribute some radiation. The emissivity of the quartz tube can also vary as a function of temperature and viewing angle. All these factors alter the temperature determined from the camera according to Eq. (13). To calibrate the temperature readings from the IR camera, experimental data was taken with thermocouples attached to surface of the tube with a ceramic adhesive. The thermocouples were located at different axial and angular positions on the tube surface. Three thermocouples were located within the area of the tube visible to the IR camera, as shown in Fig. 6(c). The thermocouples were numbered 10, 11 and 14 and will be referred to as TC10, TC11 and TC14. TC10 was located at 0.59 m and 45° from the tube centre. TC11 and TC14 are located at 0° and 0.59 m and 0.65 m, respectively, where the distance is measured from the point at which neutral gas enters the tube. Fig. 8 shows a comparison of the temperature given by the thermocouples and by the IR camera over a 60 second period. Fig. 8(a) plots the relationship between

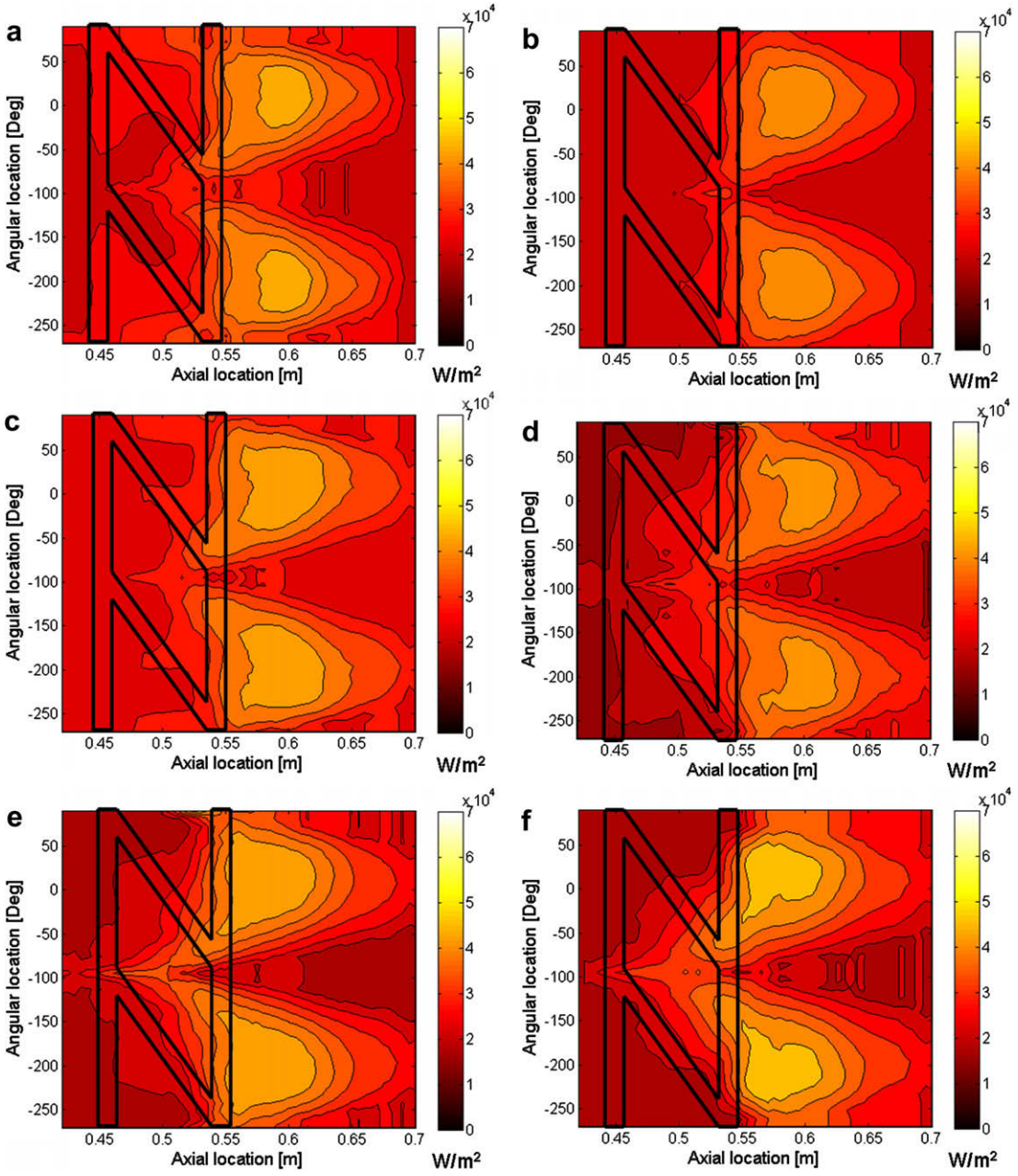

Fig. 15. Average heat flux distribution from the plasma as magnetic field distribution is varied by varying the current in M1. (a) M1: 100 A, (b) M1: 200 A, (c) M1: 300 A, (d) M1: 400 A, (e) M1: 500 A, (f) M1: 600 A.

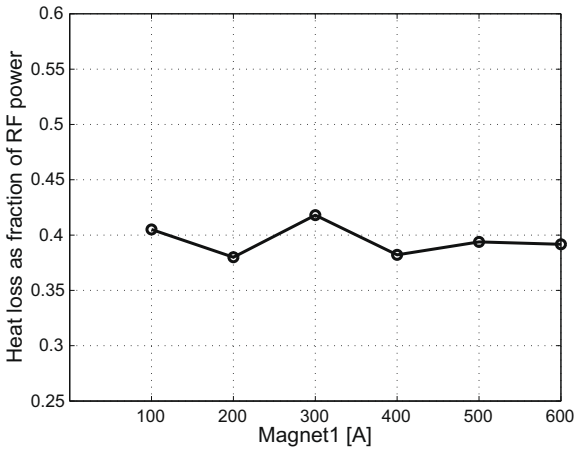

Fig. 16. Total heat load as percentage of applied heat flux versus current in M1. The observed changes are within the error of the measurement.

the camera temperature and the tube temperature using Eq. (18) for three different emissivity values

$$T_{cam} = \left(0.7\varepsilon_{IR}T_{tube}^4 + 0.3T_{amb}^4\right)^{0.25}. \quad (18)$$

The effect of viewing angle on the temperature seen by the camera is clear from Fig. 8(a), with the area at the top of the tube near TC10 appearing (from IR reading) much cooler than the centre of the tube where TC11 and TC14 are located. Over the temperature range of interest, the relationship between the temperature recorded by the IR camera and the actual temperature can be described with a linear fit. With the camera set to a 100 K range. The linear fit for the temperature relationship at locations 10, 11 and 14 is given with

TC10: $Y = 1.64T_{IR} - 149$
TC11: $Y = 1.35T_{IR} - 68$
TC14: $Y = 1.38T_{IR} - 87$

To extend this relationship for all points on the tube a 2D spline interpolation/extrapolation of the relationship at the three points is carried out. At each point on the tube surface the temperature is corrected using Eq. (19) as follows:

$$Y(\theta,z,t) = A(\theta,z) \times T_{IR}(\theta,z,t) + B(\theta,z). \quad (19)$$

The temperature data from the thermocouples is compared with the uncorrected and corrected temperature data from the IR camera in Fig. 8(b) and (c). This correction procedure resulted in the determination of a higher heat load than estimated previously [21]. The data from the thermocouples show a significant lag in the measured temperature response compared to the IR camera. In some case the thermocouples can take up to a minute to reach their maximum temperature. This is much longer than it would take for heat to diffuse through the 2.5 mm thick quartz tube. Thermocouples are attached to the tube surface using a ceramic adhesive. The data indicates that there is a significant thermal resistance between the thermocouples and the tube surface, or a significant heat capacity of the ceramic in this method.

8. Experimental results

The experimental investigation of the helicon involved varying the applied RF power at the antenna, the gas flow rate into the helicon source and the profile of the magnetic field in the axial direction. The RF power was applied in 5 s pulses for all test cases. Fig. 9(a) shows a comparison between the measured temperature Y and the estimated temperature T_e at three points (0.565 m 129.1°), (0.59 m 101.5°) and (0.615 m 83°). Fig. 9(b) shows the time dependent heat flux at the inner surface of the tube at these three points. This data was taken for an applied RF power of 6 kW. The time averaged heat flux for the full surface can be seen in Fig. 10(a). The time varying behaviour of this heat flux was found to be the same for all points and shows the closest resemblance to a constant step heat impulse for the 5 s period that the RF power is applied. Varying the operational parameters of the device was found to have a negligible effect on the time varying behaviour of the heat flux. A time response closely resembling a step change in heat flux while the RF power was applied was seen for all experimental data. However the spatial distribution of heat flux did vary significantly and for the sake of clarity the following heat flux results are presented with the time averaged spatial distribution.

8.1. Increasing applied RF power

In this set of experiments gas flow rate was kept constant at 1.167×10^{-5} m^3/s of argon gas. This flow rate was measured at standard temperature and pressure for all experiments. The power applied to the antenna was varied from 5800 to 16,200 W. The magnetic field profile was kept constant with M1 and M2 carrying 300 A and M3 carrying 1600 A, which corresponds to a magnetic field strength of 0.23 T under the centre of the helicon. Fig. 10(a)–(h) shows the time averaged heat flux from the plasma at each applied power level. The location of the helicon antenna is outlined in black in each figure. The distribution of the heat flux is seen to remain relatively constant with increasing applied power. The experimental data indicates that the location of the peak heat load remains at the same location just downstream of the helicon antenna at 0.6 m from the injection point of the neutral gas and 0° from the centre of the tube as viewed with the IR camera. A comparison of the total heat lost to the tube as measured using the IR camera data shows an approximately linear relationship with respect to the applied RF power at the helicon antenna as shown in Fig. 11(a). Table 2 also shows the waste heat load as a percentage of the applied power. The average heat load to the tube is 39.5% of the applied power. The peak heat flux to the inner surface of the tube is also seen to depend linearly on the power applied at the helicon antenna as indicated in Fig. 11(b). The standard deviation of the errors associated with the linear fit is 403 W while for the peak heat flux the standard deviation is 8 kW/m^2.

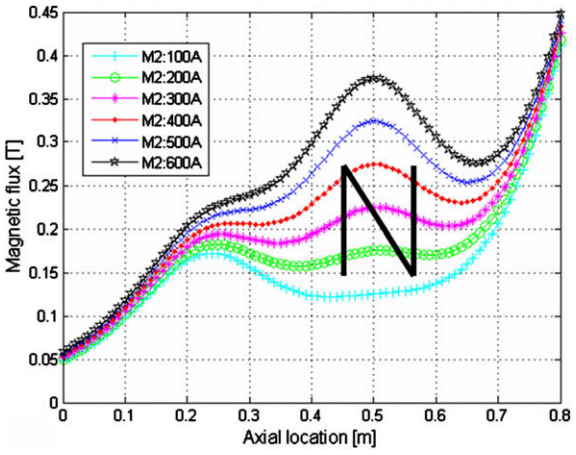

Fig. 17. Magnetic field strength versus axial location with varying M2.

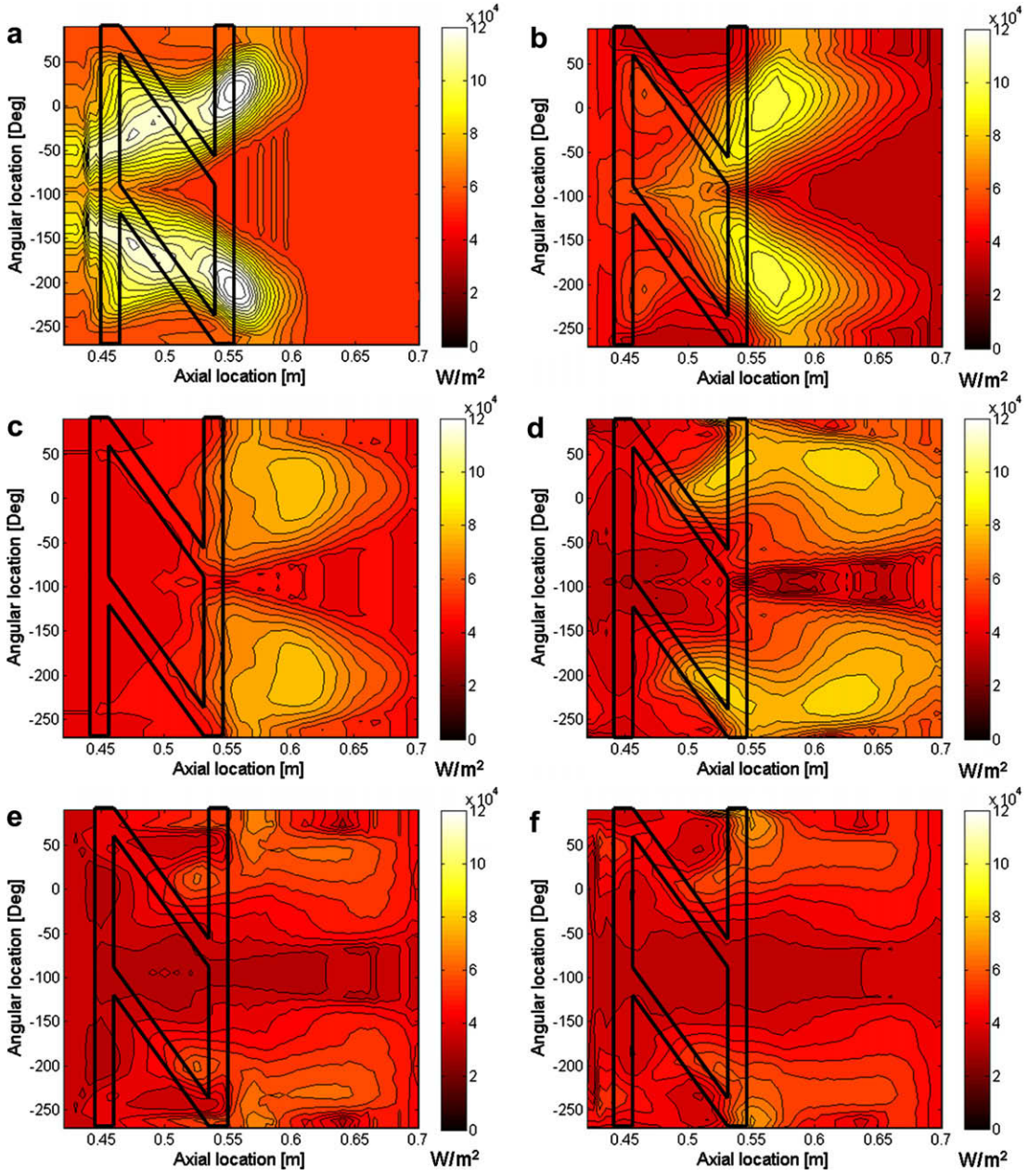

Fig. 18. Average heat flux to inner surface of tube as current in M2 is varied. (a) M2: 100 A, (b) M2: 200 A, (c) M2: 300 A, (d) M2: 400 A, (e) M2: 500 A, (f) M2: 600 A.

8.2. Varying gas flow rate

For this experiment the power applied at the RF antenna is kept constant at 12,000 W. The magnetic field is maintained with the same distribution as in Section 8.1. The neutral gas flow rate is increased from 5×10^{-6} to 1.83×10^{-5} m^3/s. The distribution of heat flux is shown in Fig. 12(a)–(e). Fig. 13 shows the total power lost as a percentage of applied RF power for varying gas flow rate. The total heat load increases as gas flow is increased although it appears to level out as the flow rate approaches 1.83×10^{-5} m^3/s. At the lowest flow rate the typical heat flux distribution changes. For this flow rate the peak heat flux occurs just under the downstream end of the helicon antenna at 0.55 m. This is perhaps indicative of capacitive coupling between the plasma and the antenna, as the antenna lies in closer proximity to the tube surface in this region due to imperfect mounting.

8.3. Varying upstream magnetic field (M1)

The magnetic field is generated by three liquid nitrogen cooled 150 turn copper coils. The variation of magnetic field of a solenoid along its central axis is given by Eq. (20)

$$B_M(z) \approx \frac{\mu_0}{4\pi} \frac{N \cdot I \cdot r_m^2}{(r_m^2 + z^2)^{3/2}}. \tag{20}$$

The axial distribution of the magnetic field for varying current in M1 is shown in Fig. 14, with the current in M2 equal to 300 A and M3 equal to 1600 A. The position of the helicon antenna is shown for reference. The power applied at the RF antenna is kept constant at 6000 W. The flow rate of the argon gas is maintained at 1.67×10^{-5} m^3/s. The heat flux distribution is shown in Fig. 15(a)–(f). Varying the current in M1 has a small effect on the

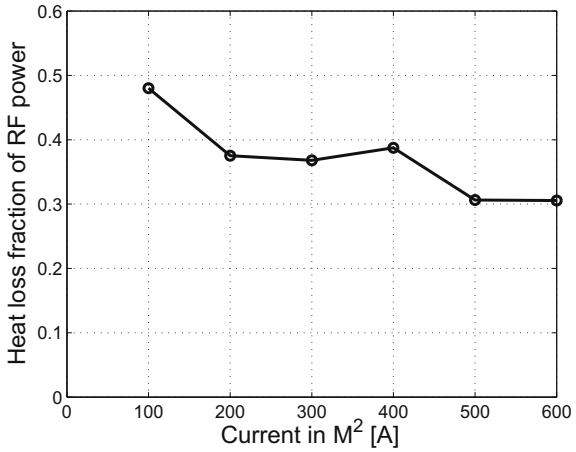

Fig. 19. Heat load as percentage of applied power versus varying current in M2.

distribution of the heat load. Fig. 16 indicates the total heat load as the current is varied. A small peak is seen in the total heat load when M1 is set to 300 A.

8.4. Varying downstream magnetic field M2

For this run of experiments M1 was kept constant with a current of 300 A. M2 was varied from 100 to 600 A. The power applied at the RF antenna was kept constant at 12,000 W, and applied for 5 s pulses. The gas flow rate was also kept constant at 1.17×10^{-5} m^3/s. The variation of the axial magnetic field as M2 is varied is shown in Fig. 17. As expected varying the current in M2 has a much larger effect on the magnetic field strength in the area which can be seen by the IR camera from 0.4 to 0.7 m than varying M1 (refer to Fig. 1). As the current in M2 is increased from 100 to 400 A the location of the peak heat flux was shifted from left to right, as shown in Fig. 18. Again as the current is increased to 500 and 600 A the location of the peak heat flux is split between 0.5 and 0.65 m. In both Fig. 18(e) and (f) localized heating can be seen occurring at the downstream edge of the helicon antenna. Fig. 19 indicates a general trend of decreasing heat load with increasing current in M2. Fig. 18(a) shows a heat being deposited across a wide area of the tube from 0.45 to 0.6 m. From Fig. 17 this length corresponds to the location of a minimal magnetic field strength. As the current in M2 is increased the local minima in the magnetic field strength shifts downstream, as does the location at which the peak heat flux to the inner surface of the tube occurs. This relationship is shown in Fig. 20(a) for 6000 W of applied power and Fig. 20(b) for 12,000 W of applied power. The axial location of the peak heat flux is marked with a hollow square. The axial variation of the magnetic field strength is also shown.

9. Conclusions

The use of the steepest descent method in solving the IHCP has been proven as an effective method for determining the waste heat flux from a high power helicon device.

The method proved capable of estimating the asymmetric heat loads that are observed during helicon operation. Temperature data obtained using thermocouples was found to have a significant lag in response time, due to thermal resistances and capacitances introduced by the method of attachment. As a result IR camera data was used as the primary measurement for the solution of the IHCP. Thermocouple measurements were used to develop a correction procedure for the IR camera data. The average heat load from the helicon was determined for a range of applied RF powers and was seen to scale linearly with power when gas flow rate and magnetic field distribution were kept constant. The average heat load was found to be close to 40% of the applied RF power. The location of the peak heat load was seen to remain constant at 0.6 m. Increasing gas flow rate was also found to increase the overall heat rejected from the plasma, although the trend indicated that saturation was reached above 1.5×10^{-5} m^3/s. The spatial distribution of the heat flux was found to depend on the type of gas used in the helicon source and the axial variation of the magnetic field strength. Changes in the magnetic field strength in the vicinity of the helicon antenna were found to have the strongest influence on the distribution of the heat rejected to the tube. Initially increasing the magnetic field strength near the antenna causes the location of the peak heat flux to shift further downstream. At field strengths above 0.3 T the location of the peak heat load was split between 0.5 and 0.65 m with localized heating occurring under the downstream strap of the antenna. Increasing the downstream magnetic field was also found to reduce the overall heat load to the helicon tube. Further experimental work will be required to establish quantitatively the relationship between the various control parameters in the helicon plasma source and the magnitude and distribution of the waste heat flux to the gas containment tube. While the heat flux is seen to behave as step

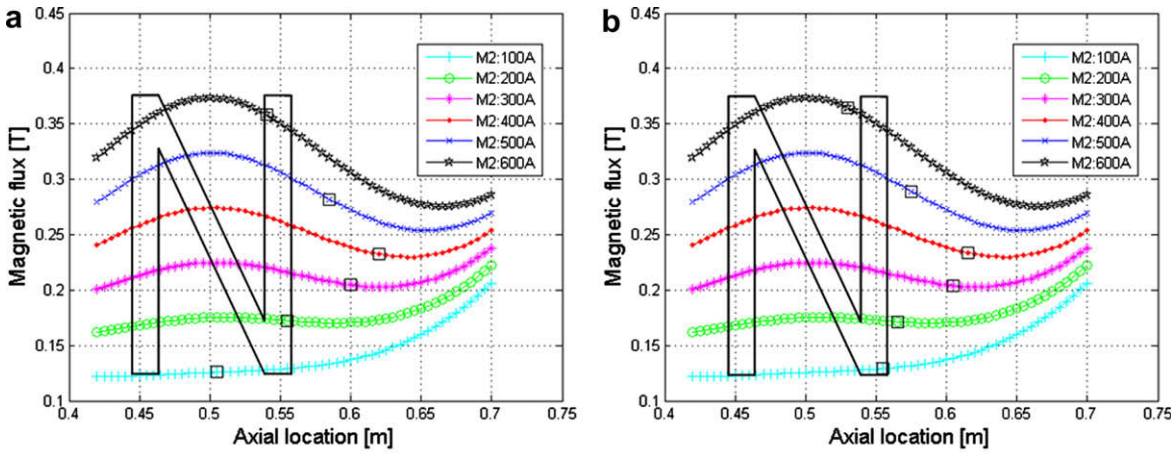

Fig. 20. Location of peak heat flux for varying magnetic field 6000 W (a). Location of peak heat flux for varying magnetic field 12,000 W (b).

response when RF power is applied for relatively short pulses, longer experimental runs will be required to determine whether the heat flux varies significantly with time.

Acknowledgement

The authors would like to acknowledge the financial support of the FÁS Science Challenge, Ireland.

References

[1] J.P. Squire, F.R. Chang-Diaz, T.W. Glover, V.T. Jacobson, G.E. McGaskill, D.S. Winter, F.W. Baity, M.D. Carter, R.H. Goulding, High power light gas helicon plasma source for VASIMR, Thin Solid Films 506–507 (2006) 579–582.
[2] R.W. Boswell, F.F. Chen, Helicons-the early years, plasma science, IEEE Trans. 25 (1997) 1229–1244.
[3] F.F. Chen, RW. Boswell, Helicons-the past decade, plasma science, IEEE Trans. 25 (1997) 1245–1257.
[4] B.N. Breizman, A.V. Arefiev, Radially localized helicon modes in nonuniform plasma, Phys. Rev. Lett. 84 (2000) 3863.
[5] G. Chen et al., Resonant power absorption in helicon plasma sources, Phys. Plasmas 13 (2006) 123507–123511.
[6] D.F. Berisford et al., Heat flow diagnostics for helicon plasmas, Rev. Sci. Instrum. 79 (2008) 10F515.
[7] J.V. Beck, B. Blackwell, C.R.J.S. Clair, Inverse Heat Conduction: Ill-Posed Problems, Wiley-Interscience, 1985.
[8] O. Alifanov, Inverse Heat Transfer Problems, Springer-Verlag, New York, 1994.
[9] J.V. Beck, B. Blackwell, A. Haji-Sheikh, Comparison of some inverse heat conduction methods using experimental data, Int. J. Heat Mass Transfer 39 (1996) 3649–3657.
[10] C. Huang, I. Yuan, H. Ay, A three-dimensional inverse problem in imaging the local heat transfer coefficients for plate finned-tube heat exchangers, Int. J. Heat Mass Transfer 46 (2003) 3629–3638.
[11] C. Huang, J. Yan, An inverse problem in simultaneously measuring temperature-dependent thermal conductivity and heat capacity, Int. J. Heat Mass Transfer 38 (1995) 3433–3441.
[12] S. Gross et al., Identification of boundary heat fluxes in a falling film experiment using high resolution temperature measurements, Int. J. Heat Mass Transfer 48 (2005) 5549–5562.
[13] Y. Yang, T. Wu, E. Wei, Modelling of simultaneous estimating the laser heat flux and melted depth during laser processing by inverse methodology, Int. Commun. Heat Mass Transfer 34 (2007) 440–447.
[14] C. Huang, S. Wang, A three-dimensional inverse heat conduction problem in estimating surface heat flux by conjugate gradient method, Int. J. Heat Mass Transfer 42 (1999) 3387–3403.
[15] M.J. Colaco, H.R.B. Orlande, Comparison of different versions of the conjugate gradient method of function estimation, Numer. Heat Transfer A Appl. 36 (1999) 229.
[16] T. Loulou, E. Artioukhine, Numerical solution of 3D unsteady nonlinear inverse problem of estimating surface heat flux for cylindrical geometry, Inverse Probl. Sci. Eng. 14 (2006) 39–52.
[17] C. Huang, H. Lo, A three-dimensional inverse problem in predicting the heat fluxes distribution in the cutting tools, Numer. Heat Transfer A Appl. 48 (2005) 1009–1034.
[18] C. Huang, H. Lo, A three-dimensional inverse problem in estimating the internal heat flux of housing for high speed motors, Appl. Therm. Eng. 26 (2006) 1515–1529.
[19] C. Gerald, P. Wheatley, Applied Numerical Analysis, Addison Wesley, 1994.
[20] H.S. Carslaw, J.C. Jaeger, Conduction of Heat in Solids, Oxford University Press, 1986.
[21] J. Mulcahy et al., Use of thermocouple and infrared camera data to compute helicon plasma source heat flux using inverse method, in: G.G.M. Stoffels, T.H. van der Meer, A.A. van Steenhoven (Eds.), Proceedings of the 5th European Conference on Thermal Sciences, Eindhoven, The Netherlands, 2008.